

# Solution NMR Characterization of Hydrogen Bonds in a Protein by Indirect Measurement of Deuterium Quadrupole Couplings

Andy C. LiWang\* and Ad Bax

Laboratory of Chemical Physics, National Institute of Diabetes and Digestive and Kidney Diseases,  
National Institutes of Health, Bethesda, Maryland 20892-0520

Received May 5, 1997

**Hydrogen bonds stabilize protein and nucleic acid structure, but little direct spectroscopic data have been available for characterizing these critical interactions in biological macromolecules. It is demonstrated that the electric field gradient at the nucleus of an amide hydrogen can be determined residue-specific by measurement of  $^{15}\text{N}$  NMR relaxation times in proteins dissolved in  $\text{D}_2\text{O}$ , and uniformly enriched with  $^{13}\text{C}$  and  $^{15}\text{N}$ . In  $\text{D}_2\text{O}$ , all backbone amide protons can be exchanged with solvent deuterons, and the  $T_1$  relaxation rate of a deuteron is dominated by its quadrupole coupling constant (QCC), which is directly proportional to the electric field gradient at the nucleus.  $^2\text{H}^{\text{N}}$   $T_1$  relaxation can be measured quantitatively through its effect on the  $T_2$  relaxation of its directly attached  $^{15}\text{N}$ . QCC values calculated from  $^2\text{H}^{\text{N}}$   $T_1$  and previously reported spectral densities correlate with the inverse cube of the X-ray crystal structure-derived hydrogen bond lengths:  $\text{QCC} = 228 + \sum_i 130 \cos \alpha_i / r_i^3$  kHz, where  $\alpha$  is the  $\text{N}-\text{H} \cdots \text{O}_i$  angle and  $r$  is the backbone-backbone ( $\text{N}-$ ) $\text{H} \cdots \text{O}_i$  ( $=\text{C}$ ) hydrogen bond distance in ångströms. © 1997 Academic Press**

recent results indicate that the amide proton chemical shift anisotropy (CSA) varies strongly with hydrogen bond strength (8). Chemical shifts are also influenced by other geometric and ring current effects, and it remains difficult to separate out the effect of hydrogen bonding, at least for the isotropic shift (9).

As the hydrogen bond is electrostatic in nature, an ideal probe of this interaction reports on its local electric environment. Deuterium possesses an electric quadrupole moment and therefore is exquisitely sensitive to its local electric environment. There are no complications from Sternheimer shielding effects (10, 11), and since its single valence is spherical, field gradients result primarily from the electrons and nuclei of nearby atoms. Qualitatively, a short  $\text{N}-^2\text{H} \cdots \text{O}=\text{C}$  hydrogen bond results in a more symmetrical electrical environment at the deuterium nucleus relative to a long hydrogen bond. That is, shorter hydrogen bonds will result in weaker electric field gradients and, therefore, smaller  $^2\text{H}$  quadrupolar coupling constant (QCC) values. Earlier  $^2\text{H}$  nuclear quadrupole resonance (NQR) and solid-state NMR studies of inorganic molecules and single (zwitterionic) amino acids deuterated at the amide site have shown that the  $^2\text{H}$  QCC follows a simple relationship of the form  $\text{QCC} = A + B/r^3$  kHz, where  $r$  is the distance between the deuterium and the acceptor group (in ångströms), and the coefficients  $A$  and  $B$  depend on the nature of the donor and acceptor (12, 13). Recent amide deuteron ( $^2\text{H}^{\text{N}}$ ) QCC measurements made by single-crystal solid-state NMR studies on small peptide analogues reiterated the tight correlation between QCC and hydrogen bond lengths determined from X-ray and neutron diffraction (14–16). These experiments inspired us to develop a method for measuring QCC values of the backbone amide deuterons ( $^2\text{H}^{\text{N}}$ ) of a protein in solution, thereby providing quantitative information on hydrogen bonding. Independently, Boyd *et al.* have developed an analogous, but technically different approach for studying  $^2\text{H}$  quadrupole couplings in  $^{15}\text{NHD}$  amino acid side chains by monitoring the  $^{15}\text{N}$  relaxation and lineshape (17).

$^2\text{H}^{\text{N}}$  relaxation in proteins is dominated by the quadrupole coupling. In principle, it is possible to measure  $^2\text{H}$  longitudi-

## INTRODUCTION

The vectorial character and the relatively weak energy of hydrogen bonds are key factors in determining the speed and specificity of enzymatic reactions (1, 2). Specific, geometrically arranged patterns of hydrogen bonds also play a critical role in determining the structure of proteins and nucleic acids. In biopolymer structures solved by either X-ray crystallography or NMR, hydrogen bonds are mostly inferred from the spatial proximity of the hydrogen bond donor and acceptor atoms after the structure has been solved using other constraints. Evidence for the presence of individual hydrogen bonds comes from protection of labile protons from hydrogen exchange with bulk solvent (3, 4). However, hydrogen exchange requires local (or global) unfolding of the polypeptide and therefore is sensitive to numerous other factors as well (5, 6). The amide proton chemical shift is also sensitive to hydrogen bonding (7), and in particular,

\* Present address: Department of Chemistry, 1393 Brown Building, 331 WTHR, Purdue University, West Lafayette, IN 47907-1393.

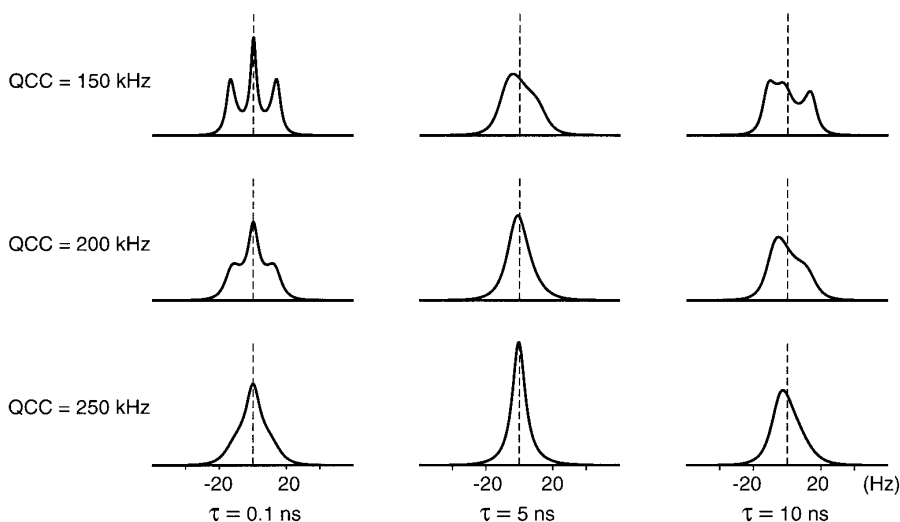


**FIG. 1.**  $^{15}\text{N}\text{-}\{^2\text{H}\}$  multiplet simulations at QCC values of 150, 200, and 250 kHz, and at  $\tau_c$  values of 0.1, 5, and 10 ns, calculated using Redfield relaxation theory (29) for isotropic rotational diffusion and  $^1J_{2\text{H-N}} = 14.4$  Hz. The  $^{15}\text{N}\text{-}\{^2\text{H}\}$  coherence evolves under the scalar coupling ( $H_J$ ), quadrupole ( $H_Q$ ), and dipolar ( $H_D$ ) Hamiltonians, and the cross correlation between  $H_Q$  and  $H_D$  (21, 22). The simulations were calculated by Fourier transformation of  $\langle I^+ \rangle = \text{Tr}\{I^+ \sigma(t)\}$ , where  $\sigma(t)$  is calculated from Eq. [5].

nal ( $T_1$ ) and transverse ( $T_2$ ) relaxation by transferring magnetization from  $^2\text{H}$  to its directly bonded  $^{13}\text{C}$  or  $^{15}\text{N}$  nucleus (18). Unfortunately, for backbone amides the sensitivity of this approach is very low and generally does not permit such experiments. However, as we demonstrate here,  $^2\text{H}^N$   $T_1$  values can be determined from the relaxation properties of the  $^{15}\text{N}$  nuclei that are  $J$ -coupled to the deuterons. Provided that the motional properties of the N–H bond vectors are known, this then allows calculation of QCC. In this work we apply this approach to a sample of uniformly  $^{13}\text{C}/^{15}\text{N}$ -enriched human ubiquitin, a small 76-residue globular protein for which a high-resolution crystal structure (19) and a detailed analysis of its rotational diffusion (20) have been published.

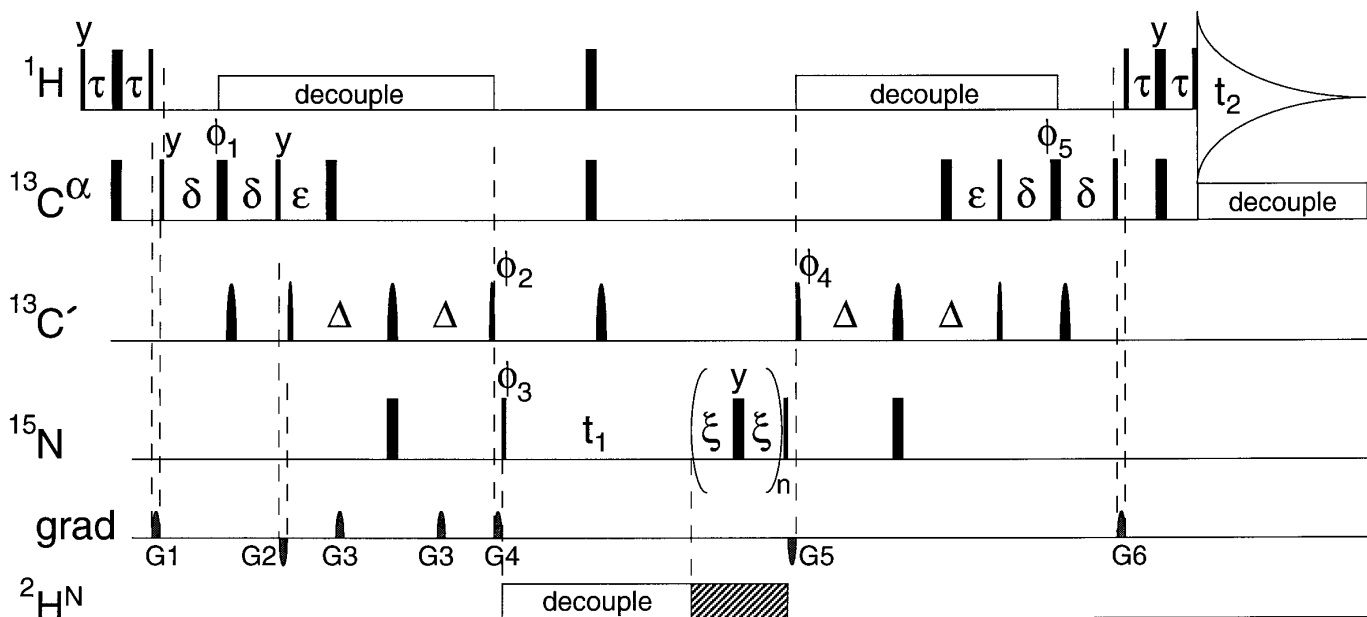
## RESULTS AND DISCUSSION

Figure 1 illustrates the exquisite sensitivity of the  $^{15}\text{N}\text{-}\{^2\text{H}^N\}$  multiplet shape to both the rotational correlation time ( $\tau_c$ ) and QCC. The triplet is resolved in the fast tumbling limit, when  $^2\text{H}^N$   $T_1$  relaxation times are much longer than  $1/{}^1J_{2\text{H-N}}$ , and collapses when  $\omega_{2\text{H}}\tau_c$  approaches 1 and the  $^2\text{H}^N$   $T_1$  values become very short. In the slow motion limit,  $\omega_{2\text{H}}\tau_c \gg 1$ , the  $^2\text{H}$   $T_1$  increases to longer than  $1/{}^1J_{2\text{H-N}}$ , and the  $^{15}\text{N}$  triplet becomes resolved again. The small degree of multiplet asymmetry observed in the slow tumbling limit results from cross correlation between the  $^{15}\text{N}\text{-}\{^2\text{H}^N\}$  dipolar and  $^2\text{H}^N$  quadrupolar relaxation mechanisms (21, 22) and has only a very small effect on the  $^2\text{H}^N$  QCC value derived from the transverse relaxation properties of the triplet (*vide infra*).

The  $^{15}\text{N}$  lineshape in a protein uniformly enriched in  $^{13}\text{C}$

and  $^{15}\text{N}$  can be observed at enhanced sensitivity by using the triple-resonance HCA(CO)N experiment (23, 24). In this two- or three-dimensional experiment, the  $^{15}\text{N}\text{-}\{^2\text{H}^N\}$  lineshape of residue  $i + 1$  is observed indirectly by using a stepwise transfer of its magnetization to  $\text{H}^\alpha$  of residue  $i$ . Rather than monitoring the  $^{15}\text{N}$  multiplet shape, a better way to obtain quantitative information on the  $^2\text{H}^N$   $T_1$  relaxation time is to measure the  $^{15}\text{N}$  transverse relaxation. In particular, the difference in  $^{15}\text{N}$  transverse relaxation rate measured in the presence and absence of  $^2\text{H}^N$  decoupling is not affected by  $^{15}\text{N}$  conformational exchange broadening,  $^{15}\text{N}$  CSA, or  $^1\text{H}\text{-}^{15}\text{N}$  or  $^{13}\text{C}\text{-}^{15}\text{N}$  dipolar couplings. There is, however, a very weak dependence of this difference on the  $^2\text{H}^N\text{-}^{15}\text{N}$  dipolar coupling, which exerts its effect through cross correlation with the  $^2\text{H}^N$  quadrupolar relaxation mechanism (*vide infra*).

Figure 2 shows the pulse scheme used in the present study. Magnetization is transferred stepwise from the sensitive  $^1\text{H}^\alpha$  spin, via the intervening  $^{13}\text{C}^\alpha$  and  $^{13}\text{C}'$  to the  $^{15}\text{N}$  spin of the next residue, in a manner similar to that of the original HCA(CO)N experiment (23). The only difference is that in the present pulse scheme, the  $^{15}\text{N}$  evolution period is followed by a Carr–Purcell–Meiboom–Gill (CPMG) spin echo train (25), prior to transfer of  $^{15}\text{N}$  magnetization back to  $\text{H}^\alpha$  of the preceding residue. The experiment is performed in a two-dimensional (2D) fashion and yields spectra with the  $^{15}\text{N}$  resonance of residue  $i + 1$  in the  $F_1$  dimension, and  $\text{H}_i^\alpha$  in  $F_2$ . The experiment is performed twice, once with  $^2\text{H}$  decoupling during the CPMG period (scheme A) and once without (scheme B). In the absence of  $^2\text{H}$  decoupling, magnetization decay strongly depends on the  $^2\text{H}^N$   $T_1$ , but in the presence of  $^2\text{H}$  decoupling it does not. To a very good ap-



**FIG. 2.** Timing diagram of the HA(CACO)N CPMG experiment. Pulses for which the phase is not indicated are applied along the  $x$  axis. Narrow and wide rectangular pulses correspond to  $90^\circ$  and  $180^\circ$  flip angles, respectively. The  $^1\text{H}$  carrier is positioned on the HDO resonance and the carriers for the  $^{13}\text{C}^\alpha$  and  $^{13}\text{C}'$  pulses are at 56 and 177 ppm, respectively. The RF field strengths of the  $90^\circ$  and  $180^\circ$   $^{13}\text{C}^\alpha$  pulses are adjusted to 4.7 and 10.6 kHz such that they do not excite the  $^{13}\text{C}'$  nuclei (for 150.9 MHz  $^{13}\text{C}$ ). Carbonyl pulse shapes correspond to the center lobe of a  $\sin x/x$  function, with durations of 157 and 84  $\mu\text{s}$  for the  $180^\circ$  and  $90^\circ$  pulses, respectively. Phase cycling is as follows:  $\phi_1 = 80^\circ, 170^\circ, 260^\circ, 350^\circ$ ;  $\phi_2 = 48^\circ$ ;  $\phi_3 = x, x, -x, -x$ ;  $\phi_4 = 132^\circ$ ;  $\phi_5 = 80^\circ$ ; acq =  $x, -x, -x, x$ . Phases  $\phi_1, \phi_2, \phi_4,$  and  $\phi_5$  are nonintegral multiples of  $90^\circ$  in order to compensate for Bloch–Siegert phase shifts, and for the change in phase associated with the change in power level on the AMX-type NMR spectrometer used. Quadrature in the  $t_1$  dimension is achieved by changing  $\phi_3$  in the usual States–TPPI manner. A 1.7-kHz RF field (2 W), centered in the amide region of the  $^2\text{H}^N$  spectrum, is used for  $^2\text{H}$  decoupling (24).  $^2\text{H}$  decoupling is applied during both  $t_1$  and the CPMG duration when collecting the reference spectrum (scheme A). In scheme B,  $^2\text{H}$  decoupling is applied only during  $t_1$ . Delay durations are  $\tau = 1.5$  ms,  $\delta = 3.1$  ms,  $\epsilon = 4.5$  ms,  $\Delta = 13$  ms, and  $\xi = 4.5$  ms. Gradient durations are  $G1 = 3$  ms,  $G2 = 1.4$  ms (negative polarity),  $G3 = 1$  ms,  $G4 = 3.3$  ms,  $G5 = 4$  ms, and  $G6 = 0.2$  ms. Pulsed field gradients are sine-bell shaped, with a peak amplitude of 25 G/cm.

proximation, the intensity ratio of a  $^{15}\text{N}$  resonance in the two spectra depends only on the QCC of its attached  $^2\text{H}^N$  and on the rotational diffusive motion of the N–H bond vector. We will first analyze  $^{15}\text{N}$  decay of magnetization in a fully classical manner, ignoring cross correlation between the  $^2\text{H}^N$ – $^{15}\text{N}$  dipolar and  $^2\text{H}^N$  quadrupolar relaxation. Following this, a description based on Redfield relaxation theory is used to demonstrate that the effect of cross correlation on the derived QCC values is very small.

*Classical description of  $^{15}\text{N}$  decay.* Evolution of transverse  $^{15}\text{N}$ – $\{^2\text{H}\}$  magnetization and relaxation during the CPMG pulse train can be described in the classical Solomon fashion (26). Using the nomenclature of Fig. 3 for the  $^{15}\text{N}$  triplet transverse magnetization vectors, the following differential equations apply:

$$\begin{aligned} dN_x^+ / dt &= W_2(N_x^- - N_x^+) \\ &+ W_1(N_x^0 - N_x^+) - 2\pi J_{2\text{H}-\text{N}}N_y^+ \quad [1a] \end{aligned}$$

$$\begin{aligned} dN_y^+ / dt &= W_2(N_y^- - N_y^+) \\ &+ W_1(N_y^0 - N_y^+) + 2\pi J_{2\text{H}-\text{N}}N_x^+ \quad [1b] \end{aligned}$$

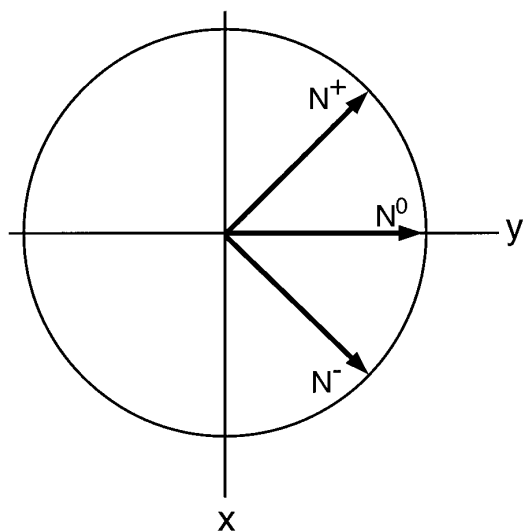


**FIG. 3.** Classical vector diagram of the dephasing of  $^{15}\text{N}$ – $\{^2\text{H}\}$  triplet components during the delay between pulses in the CPMG series of pulses.  $N^+$ ,  $N^0$ , and  $N^-$  refer to the triplet components with  $^2\text{H}$  in the  $|1\rangle$ ,  $|0\rangle$ , and  $|-1\rangle$  spin states.

$$dN_x^-/dt = W_2(N_x^+ - N_x^-) + W_1(N_x^0 - N_x^-) + 2\pi J_{2H-N}N_y^- \quad [1c]$$

$$dN_y^-/dt = W_2(N_y^+ - N_y^-) + W_1(N_y^0 - N_y^-) - 2\pi J_{2H-N}N_x^- \quad [1d]$$

$$dN_y^0/dt = W_1(N_y^- + N_y^+ - 2N_y^0), \quad [1e]$$

where (27)

$$W_1 = 3/40(QCC/\hbar)^2(1 + \eta^2/3)J(\omega_D) \quad [2a]$$

$$W_2 = 3/20(QCC/\hbar)^2(1 + \eta^2/3)J(2\omega_D) \quad [2b]$$

and where  $J_{2H-N}$  is the one-bond  ${}^2H-{}^{15}N$   $J$  coupling constant, QCC is the quadrupole coupling constant in hertz,  $J(\omega_D)$  is the real part of the spectral density function evaluated at the  ${}^2H^N$  frequency,  $\omega_D$  (cf. Eq. [6]), and  $\eta$  is the asymmetry parameter. Typically,  $0.15 \leq \eta \leq 0.22$  (16), and  $\eta^2/3 \ll 1$ , and  $\eta$  therefore is assumed to be zero in our calculations. The  $x$  components of the  ${}^{15}N$  magnetization are interchanged each time a  $180^\circ$   ${}^{15}N$  pulse is applied.

The relation between the magnitude of QCC and the decay rate of the  ${}^{15}N$  magnetization during the CPMG pulse train is analyzed by numerically integrating the five coupled differential equations (Eqs. [1]), which describe the  $x$  and  $y$  components of the three  ${}^{15}N-\{{}^2H^N\}$  multiplet components over the duration of the CPMG scheme. Figure 4A shows the decay of  $N_y$  magnetization during the CPMG spin echo train, obtained using Eqs. [1], for three different values of QCC. The decay of  ${}^{15}N$  magnetization caused by the finite lifetime of the  ${}^2H^N$  spin states is a case of scalar relaxation of the second kind (28). Besides this relaxation mechanism, the  ${}^{15}N$  transverse magnetization decays under the influence of  ${}^{15}N$  CSA,  ${}^2H-{}^{15}N$ ,  ${}^1H-{}^{15}N$  and  ${}^{13}C-{}^{15}N$  dipolar couplings, and possibly conformational exchange broadening. However, these other mechanisms affect the decay of  ${}^{15}N$  magnetization in the presence and absence of  ${}^2H^N$  decoupling equally, and therefore do not influence the intensity ratio. The solid lines in Fig. 4B show the ratios of signal intensities,  $I_B/I_A$ , observed in the absence and presence of  ${}^2H^N$  decoupling, as a function of QCC for a 94-ms CPMG period with 9.4-ms spacing between the  $180^\circ$  pulses, and rotational correlation times of 5 and 10 ns.

As mentioned above, Eqs. [1] ignore the intrinsic  $T_2$  relaxation of  ${}^{15}N$ . Although this intrinsic  $T_2$  relaxation attenuates the signals in the schemes with and without  ${}^2H^N$  decoupling identically, it decreases the signal-to-noise for both  $I_A$  and  $I_B$  and thereby increases the experimental error in  $I_B/I_A$ . It is therefore important to determine the duration of the delay,  $2\xi$ , between  $180^\circ$  pulses which maximizes the change in  $I_B$  for a small change in QCC per unit of time (Fig. 5A). Similarly, using standard values for the  ${}^{15}N$  CSA and dipolar

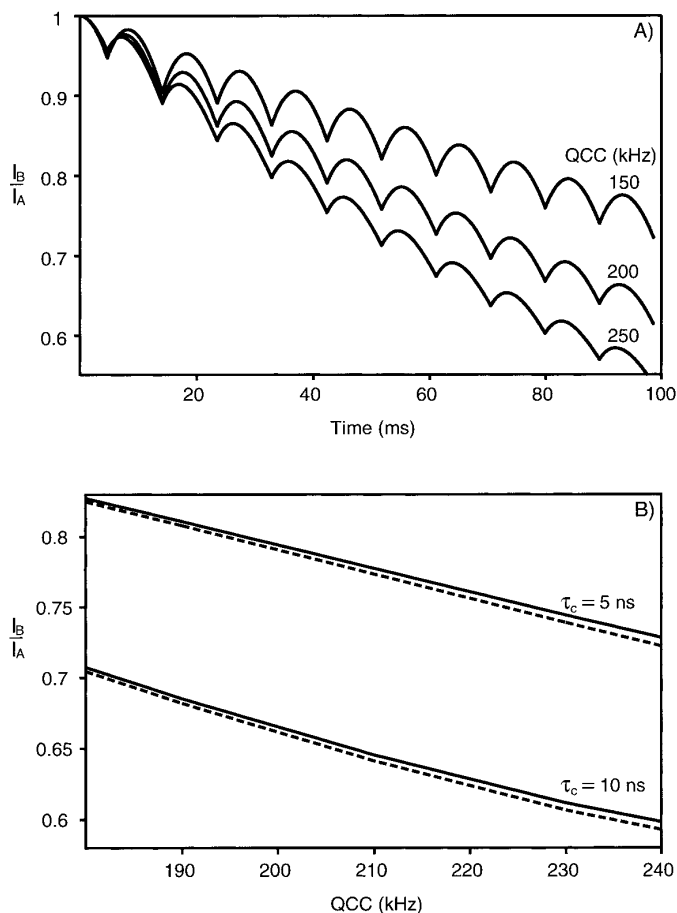


**FIG. 4.** Relation between QCC and decay rate of  ${}^{15}N$  transverse magnetization. (A) Decay of  $N_y$  magnetization due to scalar relaxation during the CPMG spin echo train without  ${}^2H^N$  decoupling, obtained using Eq. [1], for three different values of QCC, using a rotational correlation time,  $\tau_c$ , of 5 ns and a 9.4-ms spacing between  $180^\circ$  pulses. (B) Ratio of signal intensities,  $I_B/I_A$ , as a function of QCC for a total duration of the CPMG period of 94 ms and 9.4-ms spacing between the  $180^\circ$  pulses, calculated without (solid lines) and with (dashed lines) taking into account the effect of  $H_D-H_Q$  relaxation interference, for  $\tau_c = 5$  and 10 ns, and a magnetic field strength of 14 T.

interactions, one can calculate the optimal duration of the total CPMG relaxation delay (Fig. 5B).

*Semi-classical description of  ${}^{15}N$  decay.* The above description in terms of transition probabilities does not take into account effects such as relaxation interference. We therefore also provide a more complete analysis of the time evolution of the  ${}^{15}N-\{{}^2H^N\}$  spin system during the CPMG sequence, using Redfield relaxation theory (29). The density operator,  $\sigma(t)$ , evolves under the influence of the interaction frame Hamiltonian,  $H$ , where  $H = H_J + H_Q + H_D + H_{CSA} + H_{RF}$ .  $H_J$  is the one-bond scalar coupling Hamiltonian between  ${}^{15}N$  and  ${}^2H^N$ ,  $H_Q$  is the quadrupole coupling Hamiltonian of the amide deuteron,  $H_D$  is the  ${}^2H^N-{}^{15}N$  dipole-dipole Hamiltonian,  $H_{CSA}$  is the  ${}^{15}N$  chemical shift anisot-

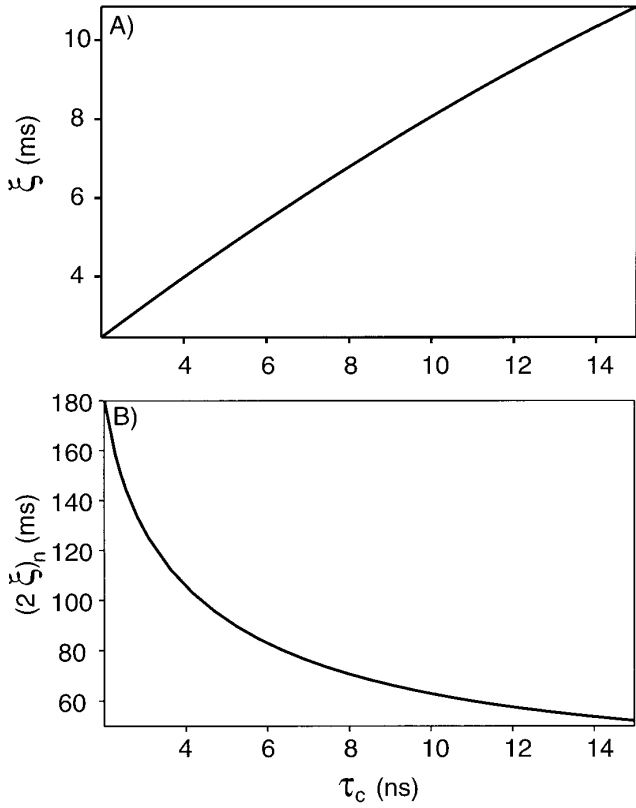


**FIG. 5.** (A) Duration of the delay  $\xi$  which maximizes the change in the observed scalar relaxation rate of the second kind ( $1/T_{2,sc}$ ) for a small change in QCC as a function of the rotational correlation time,  $\tau_c$ . (B) Optimal duration of the total CPMG relaxation when using  $\xi$  of (A), calculated using standard  $^{15}\text{N}$  CSA (160 ppm) and a  $\text{H}^{\text{N}}\text{-N}$  distance of 1.02 Å. The optimum CPMG duration,  $T$ , is obtained by maximizing the derivative of  $[1 - \exp(-T/T_{2,sc})\exp(-T/T_{2,intr})]$  with respect to QCC, where  $1/T_{2,intr}$  is the intrinsic relaxation rate caused by dipolar and CSA interactions.

ropy Hamiltonian, and  $H_{\text{RF}}$  represents the interaction between  $^2\text{H}^{\text{N}}$  and the on-resonance radiofrequency field (used to decouple  $^2\text{H}$  from  $^{15}\text{N}$  in the reference experiment). As mentioned above, information on the quadrupole coupling is contained in the ratio of resonance intensities in two spectra, collected for a given total duration of the CPMG relaxation period, in the presence (reference spectrum) and absence (attenuated spectrum) of  $^2\text{H}^{\text{N}}$  decoupling. As  $H_{\text{CSA}}$  attenuates the signals in both spectra identically this term can be omitted from the calculations. For the same reason,  $H_{\text{D}}$  concerns us only in its contribution to the quadrupole-dipolar cross correlation effect. The pertinent Hamiltonians are listed below (21):

$$H_{\text{J}} = 2\pi J_{2\text{H-N}} I_z S_z \quad [3a]$$

$$H_{\text{Q}}(t, \Omega)$$

$$= \sum_{m=-2}^2 \sum_{\alpha} {}^{\text{Q}}G {}^{\text{Q}}X_m^{\alpha} Y_2^{-m}({}^{\text{Q}}\Omega) (-1)^m \exp(i {}^{\text{Q}}\omega_m^{\alpha} t), \quad [3b]$$

$$H_{\text{D}}(t, \Omega) = \sum_{m=-2}^2 \sum_{\alpha} {}^{\text{D}}G {}^{\text{D}}X_m^{\alpha} Y_2^{-m}({}^{\text{D}}\Omega) (-1)^m \exp(i {}^{\text{D}}\omega_m^{\alpha} t), \quad [3c]$$

and

$$H_{\text{RF}} = \omega_1 S_x \quad [3d]$$

in the reference spectrum, and  $H_{\text{RF}} = 0$  in the attenuated spectrum. In the above equations,  ${}^{\text{D}}G = -(24\pi/5)^{1/2} \gamma_I \gamma_S \hbar / r^3$ ,  ${}^{\text{Q}}G = (4\pi/5)^{1/2} e^2 q Q / (4\hbar)$ ,  $Y_{2m}$  is a second-order spherical harmonic at the Euler angles  $\Omega = (\theta(t), \phi(t))$  which describe the orientation of the unique principal axis of the quadrupolar ( ${}^{\text{Q}}\Omega$ ) or dipolar ( ${}^{\text{D}}\Omega$ ) interaction relative to the external magnetic field,  $\omega_1$  is the strength of the  $^2\text{H}^{\text{N}}$  decoupling field, applied along the  $x$  axis, and  $X_m^{\alpha}$  is the spin-dependent part of the Hamiltonian (21):

$$\begin{aligned} {}^{\text{D}}X_0^1 &= (2/\sqrt{6}) I_z S_z; & {}^{\text{D}}\omega_0^1 &= 0 \\ {}^{\text{D}}X_0^2 &= -(1/2\sqrt{6}) I_- S_+; & {}^{\text{D}}\omega_0^2 &= \omega_S - \omega_I \\ {}^{\text{D}}X_0^3 &= -(1/2\sqrt{6}) I_+ S_-; & {}^{\text{D}}\omega_0^3 &= \omega_I - \omega_S \\ {}^{\text{D}}X_1^1 &= -(1/2) I_z S_+; & {}^{\text{D}}\omega_1^1 &= \omega_S \\ {}^{\text{D}}X_1^2 &= -(1/2) I_+ S_z; & {}^{\text{D}}\omega_1^2 &= \omega_I \\ {}^{\text{D}}X_2^1 &= (1/2) I_+ S_+; & {}^{\text{D}}\omega_2^1 &= \omega_I + \omega_S \\ {}^{\text{Q}}X_0^1 &= 2S_z^2 - (1/2)(S_+ S_- + S_- S_+); & {}^{\text{Q}}\omega_0^1 &= 0 \\ {}^{\text{Q}}X_1^1 &= -(3/2)^{1/2} (S_z S_+ + S_+ S_z); & {}^{\text{Q}}\omega_1^1 &= \omega_S \\ {}^{\text{Q}}X_2^1 &= (3/2)^{1/2} S_z^2; & {}^{\text{Q}}\omega_2^1 &= 2\omega_S \\ X_m^{\alpha\dagger} &= (-1)^m X_{-m}^{\alpha}; & \omega_m^{\alpha} &= -\omega_{-m}^{\alpha} \text{ for } m \neq 0, \end{aligned}$$

where  $I$  and  $S$  denote the  $^{15}\text{N}$  and  $^2\text{H}$  spin operators, and  $X^{\dagger}$  is the Hermitian adjoint of the operator  $X$ .

The Liouville equation of motion for  $\sigma(t)$ , during the  $2\xi$  delay periods, in the interaction representation is

$$d\sigma(t)/dt = (-i\underline{H}_{\text{J}} - i\underline{H}_{\text{RF}} - \underline{\Gamma})\sigma(t), \quad [4]$$

with

$$\begin{aligned} \underline{\Gamma} &= 1/4\pi \sum_{m=-2}^2 \sum_{\alpha, \alpha', I, I'} {}^I G {}^{I'} G {}^I \underline{X}_m^{\alpha} {}^{I'} \underline{X}_m^{\alpha'\dagger} \\ &\times P_2(\cos \theta_{\text{II}'} ) J({}^I \omega_m^{\alpha}), \end{aligned}$$

where  $I$  and  $I'$  refer to either Q or D. Underscores denote superoperators, and  $\underline{X}$ ,  $\underline{H}_{\text{RF}}$ , and  $\underline{H}_{\text{J}}$  are the commutator superoperators of  $X$ ,  $H_{\text{RF}}$ , and  $H_{\text{J}}$ .  $P_2$  is the second-order Legendre polynomial and  $\theta_{\text{II}'}$  is the angle between the unique principal axes of  $I$  and  $I'$ . The secular approximation ( ${}^I \omega_m^{\alpha}$

$= {}^I\omega_m^{\alpha'}$ ) has been made and  $J({}^I\omega_m^{\alpha'})$  refers to the complex spectral density at frequency  ${}^I\omega_m^{\alpha'}$  (cf. Eq. [6]). The solution to Eq. [4] is  $\sigma(t) = \exp[(-i\mathbf{H}_J - i\mathbf{H}_{\text{RF}} - \mathbf{\Gamma})t]\sigma(0+)$ , where  $\sigma(0+)$  is the density matrix at the start of the CPMG period. The  ${}^{15}\text{N}-\{{}^2\text{H}^{\text{N}}\}$  magnetization after a  ${}^{15}\text{N}$  CPMG pulse train consisting of  $n$   ${}^{15}\text{N}$   $180^\circ$  pulses spaced by  $2\xi$  is described by

$$\begin{aligned} & \sigma[n(2\xi + |P_y(180^\circ)|)] \\ &= \{\exp[(-i\mathbf{H}_J - i\mathbf{H}_{\text{RF}} - \mathbf{\Gamma})\xi] \cdot P_y(180^\circ) \\ & \quad \times \exp[(-i\mathbf{H}_J - i\mathbf{H}_{\text{RF}} - \mathbf{\Gamma})\xi]\}^n \sigma(0+), \end{aligned} \quad [5]$$

where  $|P_y(180^\circ)|$  is the duration of the  $180^\circ$  pulse,  $P_y(\theta) = \exp(-i\theta I_y)$ . Evolution of the density matrix is restricted to a subspace of the full Liouville space. Therefore, a set of orthogonal basis operators can be used to represent the density matrix:  $\sigma(t) = \sum_k b_k(t)B_k$ , where  $B_k$  belongs to the 18-member basis set  $\mathbf{B} = \{I^\pm S^{ij}\}$  ( $i, j = -1, 0, 1$ ) and  $S^{ij}$  is the matrix element connecting state  $j$  to state  $i$  for spin  $S$  ( $S^{ij} = |i\rangle\langle j|$ ). The transverse magnetization immediately following the CPMG pulse train is then given by  $\langle I^+ \rangle = \text{Tr}\{I^+ \sigma[n(2\xi + |P_y(180^\circ)|)]\}$  and is evaluated by means of a computer program.

The dashed lines in Fig. 4B show the ratio of signal intensities,  $I_B/I_A$ , observed in the absence and presence of  ${}^2\text{H}^{\text{N}}$  decoupling, as a function of QCC. These ratios are calculated using Eq. [5], again for isotropic diffusion with a rotational correlation time of either 5 or 10 ns, and a magnetic field strength of 14 T. As can be seen from comparing the results obtained without consideration of the cross correlation effect (solid lines), the effect of cross correlation on the intensity ratio,  $I_B/I_A$ , is very small and results in a slightly lower ratio for a given QCC value.

The rotational diffusion of ubiquitin to a good approximation is axially symmetric (20) and, in addition, the N–H bond vectors are subject to rapid internal motion. For this case, the complex spectral density function can be approximated by (22)

$$\begin{aligned} J(\omega) &= S^2 \sum_{k=1}^3 A_k [(\tau_k + i\omega\tau_k^2)/(1 + \omega^2\tau_k^2)] \\ & \quad + (1 - S^2)[\tau_e/(1 + \omega^2\tau_e^2)], \end{aligned} \quad [6]$$

where  $A_1 = (1.5 \cos^2\beta - 0.5)^2$ ,  $A_2 = 3 \sin^2\beta \cos^2\beta$ ,  $A_3 = 0.75 \sin^4\beta$ ,  $\beta$  is the angle between the N–H bond vector and the cylinder axis,  $S^2$  is the generalized order parameter for internal motion (30),  $\tau_e$  is the correlation time for internal motion, and the time constants are  $\tau_1 = (6D_\perp)^{-1}$ ,  $\tau_2 = (D_\parallel + 5D_\perp)^{-1}$ ,  $\tau_3 = (4D_\parallel + 2D_\perp)^{-1}$ .  $D_\perp$  and  $D_\parallel$  are the perpendicular and parallel diffusion constants of ubiquitin. The residue-specific  $\beta$  angles and  $S^2$  and  $\tau_e$  values were

taken from Tjandra *et al.* (20). The rotational diffusion constants of Tjandra *et al.*,  $D_\parallel$  and  $D_\perp$ , were scaled for the lower temperature and the change in  $\text{H}_2\text{O}/\text{D}_2\text{O}$  isotopic ratio, using a  $\text{D}_2\text{O}$  viscosity of 1.09 cp at  $25^\circ\text{C}$  in the present work (31). All analyses of the experimental data were carried out using Eqs. [5] and [6].

*Application to ubiquitin.* The experiment of Fig. 2 was applied to a sample of  ${}^{13}\text{C}/{}^{15}\text{N}$ -enriched human ubiquitin, dissolved in  $\text{D}_2\text{O}$ . Small regions taken from the two spectra collected with and without  ${}^2\text{H}$  decoupling are shown in Fig. 6. The two spectra were acquired in an interleaved manner rather than sequentially. This minimizes the effects of slow changes in spectrometer hardware or sample conditions, which might occur during the course of the experiment, on the intensity ratio of the two spectra. Thus, data with and without  ${}^2\text{H}^{\text{N}}$  decoupling are acquired and stored separately, prior to incrementation of the  $t_1$  evolution period. The peak intensity differences between resonances in the two spectra therefore result exclusively from the faster  ${}^{15}\text{N}$  decay in the absence of  ${}^2\text{H}$  decoupling during the CPMG pulse train. Because Pro has no amide hydrogen, it is expected to show identical resonance intensities with and without  ${}^2\text{H}$  decoupling. As can be seen for Pro<sup>37</sup> in Fig. 6, this is confirmed experimentally.

Four experiments (i.e., four pairs of spectra) were conducted with CPMG pulse train lengths of 91, 127.3, 145.5, and 145.5 ms, and  $2\xi$  durations of 9.1 ms. For each  ${}^{15}\text{N}_{i+1}/{}^1\text{H}_i^\alpha$  correlation in a given experiment, the ratio of its intensity from pulse scheme B,  $I_B$ , over that from pulse scheme A,  $I_A$ , was obtained. Calculating the  ${}^2\text{H}$  QCC from  $I_B/I_A$  was carried out by calculating the evolution of the density matrix (Eq. [5]) over the duration of the CPMG pulse train in both the presence and absence of  ${}^2\text{H}^{\text{N}}$  decoupling, for a series of different QCC values. Comparison of the experimental  $I_B/I_A$  ratio with this array of simulated  $I_B/I_A$  ratios then yields QCC. Calculations were repeated for each residue, using residue-specific  ${}^1J_{2\text{H}-\text{N}}$  values ( ${}^1J_{2\text{H}-\text{N}} = \gamma_{2\text{H}}/\gamma_{1\text{H}}{}^1J_{1\text{H}-\text{N}}$ ), taken from Ref. (32), and internal dynamics parameters ( $S^2$ ,  $\tau_i$ ) and orientations of the N–H bond vectors in the frame of the axially symmetric rotational diffusion tensor, taken from Ref. (20).

For 4 of the 65 observed nonprolyl backbone amides no information on mobility and  ${}^1J_{\text{HN}}$  was available, one of the observed  $\text{H}^\alpha$  overlaps with residual HDO solvent signal, and for 13 residues the  ${}^{15}\text{N}-\{{}^1\text{H}\}$  NOE value is  $<0.7$ . Low NOE values correspond to considerable mobility on a timescale in the nanosecond range, which increases the uncertainty in  $J(\omega_D)$  and  $J(2\omega_D)$ , thereby increasing the error in QCC. The reproducibility of the QCC value derived for Asn<sup>60</sup> in four separate measurements was much poorer than for other residues, and Asn<sup>60</sup> is therefore not considered in the further analysis. This leaves 46 reliable QCC values. Of these, 30 are involved in single backbone–backbone hydrogen bonds,

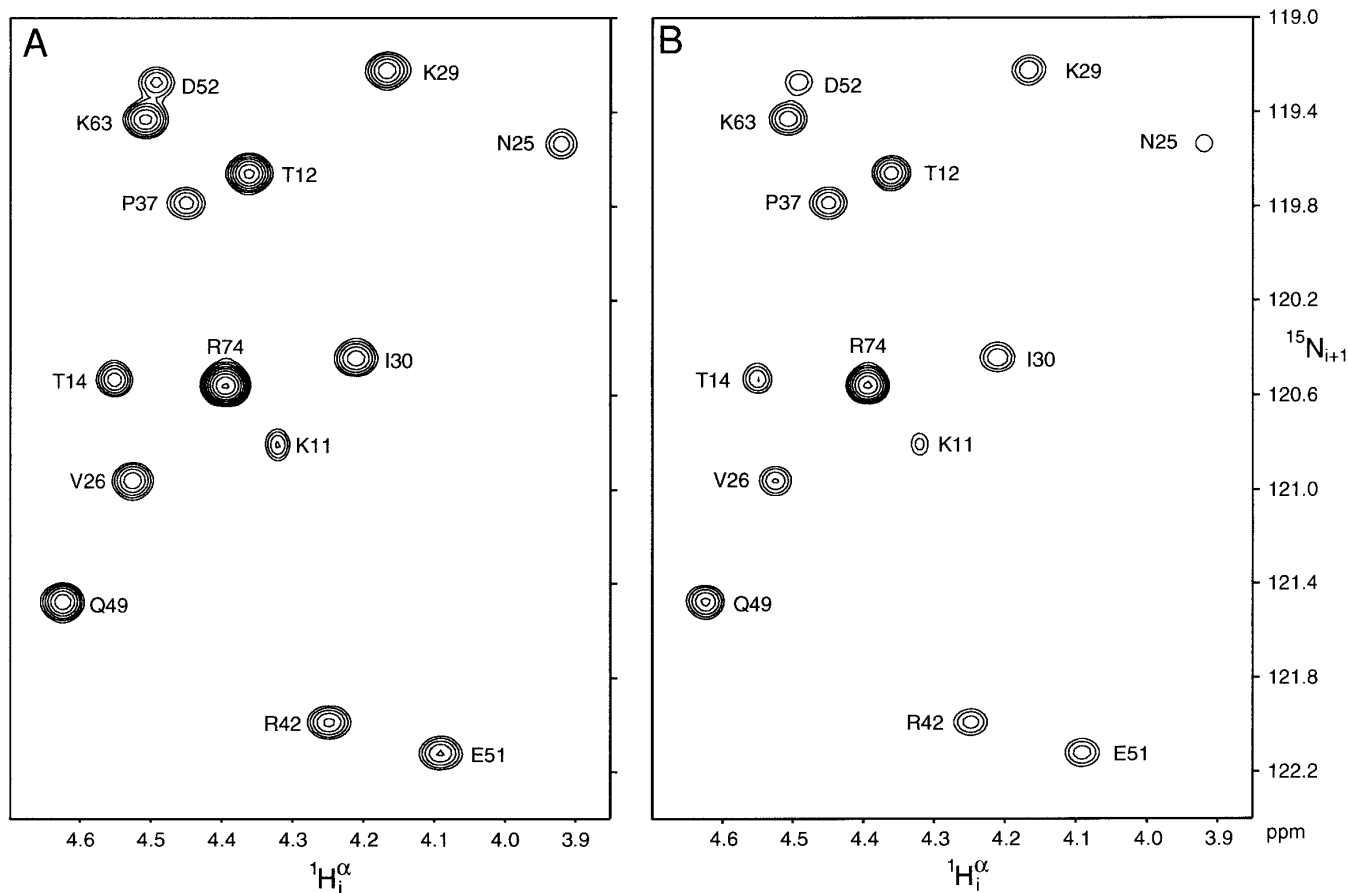


**FIG. 6.** A small region of the reference (A) and attenuated (B) spectra of ubiquitin using a CPMG pulse train length of 127 ms. Data were collected in an interleaved manner, thereby minimizing the effects of spectrometer instability on the relative intensity of the two spectra. Both spectra were acquired as  $416^* \times 768^*$  data matrices, with acquisition times of 266 ms ( $t_1$ ,  $^{15}\text{N}$ ) and 80 ms ( $t_2$ ,  $^1\text{H}^\alpha$ ). Contours are spaced by a factor of 1.35.

3 are hydrogen bonded to a side chain oxygen, 5 are within hydrogen bonding distance ( $3 \text{ \AA}$ ) and angle ( $>120^\circ$ ) of two oxygens, and 4 are hydrogen bonded to a water oxygen. For 4 amides, there is no hydrogen bonding partner in the crystal structure, although 3 of them have solvent accessible surface areas greater than 20% (as probed by a  $1.4\text{-\AA}$  sphere, using X-PLOR) and presumably form a hydrogen bond to water. QCC values are presented in Table 1 and values range from 199 to 227 kHz. As can be seen from Fig. 4B, use of the classical Solomon-type description would result in QCC values that are larger by about 2 kHz.

The ubiquitin crystal structure indicates that all but one (Thr<sup>22</sup>) of the amides with  $\text{NOE} \geq 0.7$  considered above are either involved in one or two hydrogen bonds or are exposed to the solvent. Except for Thr<sup>22</sup> and Ile<sup>36</sup> (which is preceded by Gly and no QCC value could be measured), all non-solvent-exposed amides for which no clear hydrogen bonding partner can be discerned in the crystal structure have  $\text{NOE} < 0.7$  and show increased internal dynamics. These very weakly or nonhydrogen bonded amides show

QCC values which are uniformly higher, in the range 224–236 kHz.

Based on the reproducibility of four separate measurements, the root-mean-square uncertainty in the resulting averaged QCC values is  $\pm 2.8$  kHz. This error does not include uncertainties in the dynamics parameters or in the orientation of the N–H vector relative to the diffusion tensor.

*Correlation between QCC and hydrogen bonding.* Hydrogen bond lengths and angles were obtained from the  $1.8\text{-\AA}$  ubiquitin crystal structure (19), with protons built on by the program X-PLOR (33).

Figure 7 shows the correlation between QCC and the hydrogen bond length and angle derived from the crystal structure. The solid line is the best fit and corresponds to

$$\text{QCC} = 228 + \sum_i 130 \cos \alpha_i / r_i^3 \text{ kHz}, \quad [7]$$

where  $r_i$  is the (N–)H to  $\text{O}_i(=\text{C})$  distance in  $\text{\AA}$ , and  $\alpha_i$  is the N–H $\cdots\text{O}_i$  hydrogen bond angle. To first

**TABLE 1**  
**Quadrupole Coupling Constants Derived for Backbone Amide Deuterons in Human Ubiquitin,**  
**Together with Hydrogen Bond Distance and Angles Taken from the Crystal Structure<sup>a</sup>**

H <sup>N</sup>	QCC (kHz)	Acc1	Atom	r <sub>O-H</sub> (Å)	α (°)	Acc2	Atom	r <sub>O-H</sub> (Å)	α (°)
I3	213.5	L15	O	2.09	166				
F4	206.4	S65	O	1.90	165				
V5	211.7	I13	O	1.85	162				
K6	210.9	L67	O	1.94	168				
T7	212.1	K11	O	1.94	169				
T14	210.4	S <sup>b</sup>							
L15	211.2	I3	O	2.08	168				
V17	204.5	M1	O	1.88	174				
E18	199.7	D21	O <sup>δ2</sup>	2.11	169				
T22	224.4	None <sup>c</sup>							
I23	208.9	R54	O	1.94	156				
V26	219.8	T22	O	2.19	157				
K27	207.2	I23	O	2.04	165				
A28	218.8	E24	O	2.20	150				
K29	218.5	N25	O	2.02	154				
I30	210.3	V26	O	2.08	152				
Q31	220.3	K27	O	2.03	152				
D32	208.0	A28	O	1.90	168				
K33	209.7	K29	O	2.05	146	I30	O	2.69	120
E34	206.0	I30	O	1.98	159				
G35	218.3	I30	O	2.92	128	Q31	O	1.96	135
D39	219.8	W4 <sup>d</sup>	O	1.94					
Q40	213.3	P37	O	2.04	156				
Q41	219.9	P38	O	2.21	152				
R42	216.0	V70	O	1.97	143				
L43	210.6	W28 <sup>d</sup>	O	1.93					
I44	213.2	H68	O	1.85	160				
F45	219.5	K48	O	2.11	165				
A46	219.8	W2 <sup>d</sup>	O	2.12					
G47	214.1	W27 <sup>d</sup>	O	1.95					
L50	207.4	L43	O	1.86	171				
E51	212.9	Y59	OH	2.06	153				
D52	209.4	S <sup>b</sup>							
T55	206.7	D58	O <sup>δ1</sup>	2.12	167				
L56	212.3	D21	O	2.09	151				
S57	215.3	P19	O	1.98	145				
D58	216.2	T55	O	2.38	131	T55	O <sup>γ1</sup>	2.43	143
Y59	216.2	T55	O	2.99	148	L56	O	2.36	132
I61	221.8	L56	O	2.46	165				
E64	208.1	Q2	O	1.86	156				
S65	216.1	Q62	O	2.43	138				
T66	213.9	S <sup>b</sup>							
L67	208.3	F4	O	1.88	159				
H68	207.1	I44	O	1.82	172				
L69	214.5	K6	O	1.95	173				
V70	204.7	R42	O	1.85	165				

<sup>a</sup> Only residues with an <sup>15</sup>N-<sup>1</sup>H NOE ≥ 0.7 have been included. Hydrogen bond partners are only listed for α ≥ 120° and r<sub>O-H</sub> ≤ 3 Å.

<sup>b</sup> Solvent accessible (>20%) and very fast hydrogen exchange.

<sup>c</sup> Solvent accessibility ~8%; slow hydrogen exchange.

<sup>d</sup> Crystallographically observed water oxygen.

order, the cos α factor accounts for the nonlinearity of the hydrogen bond (assuming axial symmetry of the <sup>2</sup>H<sup>N</sup> quadrupole coupling in the absence of hydrogen bonding). Al-

though cos α is relatively uniform, the correlation coefficient, R, improves from 0.60 when using the original equation (12, 13) lacking this factor, to 0.74 when including it.

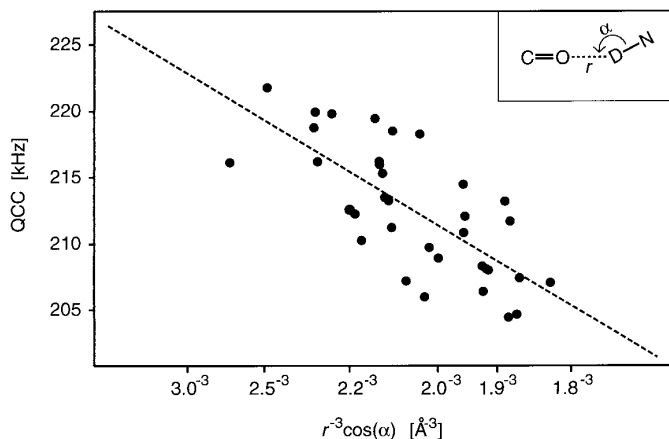


**FIG. 7.** Correlation of  $^2\text{H}^{\text{N}}$  QCC values and inverse cube hydrogen bond distances for ubiquitin. Only amides with restricted internal motions ( $^{15}\text{N}-\{^1\text{H}\}$  NOE  $\geq 0.7$ ) are included. The QCC values represent averages over four experiments and, based on their reproducibility, have an average root-mean-square error of 2.8 kHz; only residues for which the rms uncertainty in QCC is smaller than 5 kHz are included. The uncertainty in the hydrogen bond lengths is estimated to be about 0.15 Å. Data for 35 backbone amides involved in either single or bifurcated backbone-backbone hydrogen bonds are represented by filled circles. The dashed line represents the best fit between the filled circles (backbone-backbone hydrogen bonds) and the equation  $\text{QCC} = A + \sum_i B \cos \alpha_i / r_i^3$  kHz, where  $r_i$  is the (N-H)···O(=C) hydrogen bond distance in ångströms,  $\alpha_i$  is the N-H···O<sub>i</sub> angle, and  $A = 228 \pm 2.5$  kHz,  $B = 130 \pm 21$  kHz. Only oxygens for which  $\alpha > 120^\circ$  and  $r_i \leq 3$  Å are included in the summation. The rms deviation of the fit is 3 kHz.

Equation [7] is entirely empirical. One would expect (11) the effect of the nonlinearity of the hydrogen bond to result in an equation of the type  $\text{QCC} = A + B \sum_i P_2(\cos \alpha_i)$ , with  $P_2(\cos \alpha_i) = (3 \cos^2 \alpha_i - 1)/2$ . Fitting this latter equation results in  $A = 221$  and  $B = -89$ . The correlation coefficient,  $R$ , decreases to 0.70, however, suggesting that it is slightly less good in correlating QCC with hydrogen bond lengths and angles than Eq. [7]. The reason why QCC is less sensitive to the hydrogen bond angle than that predicted by a  $P_2(\cos \alpha)$  dependence may originate in part from the increase in the asymmetry parameter,  $\eta$ , which would increase with the deviation from linearity of the hydrogen bond. It may also reflect a correlation between the average local electrical polarizability and the angle  $\alpha$ .

Equation [7] is consistent with previous QCC values obtained for model peptides using single-crystal, solid-state NMR. Gerald *et al.* (15) determined the quadrupole coupling tensor for the amide of the model peptide *N*-acetyl-D,L-valine and found a  $(\sqrt{S^2}) \times \text{QCC}$  of 212.6 kHz for a (N-H) to O(=C) distance of 2.32 Å and  $\alpha = 159^\circ$ , where  $S^2$  is the generalized order parameter which is related to the amplitude of fast internal motions (30). Note that QCC values obtained in the present study have already been corrected for the effect of internal dynamics, and Eq. [7] therefore refers to the case where there is no internal motion. Thus, the 218-

kHz QCC value predicted by Eq. [7] for a hydrogen bond length of 2.32 Å corresponds to a  $\sqrt{S^2} \times 218$  kHz = 212.6 kHz quadrupole splitting in the solid-state NMR spectrum, yielding  $S^2 = 0.95$ . This  $S^2$  value is consistent with previously published values (34). In a second single-crystal NMR study of *N*-acetylglucine (14) a  $(\sqrt{S^2}) \times \text{QCC}$  of 210 kHz was measured for the amide deuteron which was intermolecularly hydrogen bonded to the glycyl carbonyl oxygen at a distance of 2.14 Å, with  $\alpha = 173^\circ$ . Equation [7] predicts a QCC of 215 kHz, which again indicates  $S^2 = 0.95$ .

Previous parametrizations of Eq. [7] were performed on either small inorganic molecules (12) or single amino acids, some of which were zwitterions (13). The new parametrization of Eq. [7] represents the first calibration of QCC versus  $r$  for amide deuterons in proteins. It differs substantially from the earlier parametrizations because of the different acceptor and donor groups used in the earlier studies. Indeed, hydrogen bonding to a charged carboxyl side chain decreases the QCC value more than a hydrogen bond to a backbone carbonyl, and the smallest QCC value (199.7 kHz) in ubiquitin is found for the amide of Glu<sup>18</sup>, hydrogen-bonded to the carboxyl of Asp<sup>21</sup>. The only other amide in ubiquitin also hydrogen bonded to a side chain carboxylate (Thr<sup>55</sup> to Asp<sup>58</sup> O<sup>δ</sup>) also yields a very small QCC value of 206.7 kHz.

The largest QCC values are found for the amides of Thr<sup>9</sup> (236 kHz) and Lys<sup>11</sup> (233 kHz), both forming weak hydrogen bonds ( $r_{\text{H-O}} = 2.4$  and 2.7 Å) to Thr<sup>7</sup>-O<sup>γ</sup> in the X-ray structure, with no solvent accessibility. Both amides also are subject to substantial internal dynamics (NOE  $\sim 0.66$ ;  $S^2 \approx 0.72$ ) and fast hydrogen exchange, confirming the weakness of these hydrogen bonds, but also increasing the uncertainty in the derived QCC values because of the higher uncertainty in  $J(\omega_{\text{D}})$  and  $J(2\omega_{\text{D}})$ .

For four relatively rigid, solvent-exposed amides that are all hydrogen bonded to water oxygens in the crystal structure (Asp<sup>39</sup>, Leu<sup>43</sup>, Ala<sup>46</sup>, and Gly<sup>47</sup>), QCC values fall in the range 211–220 kHz. QCC values for three other nonflexible amides with a solvent accessibility greater than 20% (Thr<sup>14</sup>, Asp<sup>52</sup>, and Thr<sup>66</sup>) but not hydrogen bonded to a water molecule in the X-ray structure, fall in the range 209–214 kHz. This suggests that there is no correlation between the magnitude of QCC and the presence or absence of a hydrogen-bonded water molecule in the X-ray structure. The absence of a water molecule in the crystal structure for these solvent-exposed amides presumably reflects a wider distribution in the position of the hydrogen bonding water molecule, and not a weakness of hydrogen bonding.

## CONCLUDING REMARKS

We have shown that individual backbone amide QCC values in proteins can be measured by solution NMR. Our study confirms that amide deuteron quadrupole couplings are quite sensitive to hydrogen bonding and thereby provide

unique spectroscopic probes for studying this interaction in solution. However, our data also indicate that  $H^N$  QCC values of peptide amides are quite uniform and clearly show that no strong hydrogen bonds are present in ubiquitin. This is confirmed by the narrow range of amide proton/deuterium fractionation factors reported for this protein (35).

Precise measurement of QCC requires accurate knowledge of the spectral densities applicable to the rotational diffusion of the individual N–H bond vectors, and also accurate measurement of the  $^1J_{NH}$  (and thereby  $^1J_{ND}$ ) scalar coupling. Indeed, without taking the anisotropic rotational diffusion into account, or without using residue-specific  $^1J_{ND}$  values, the correlation between QCC and hydrogen bond length virtually disappears ( $R < 0.5$ ; data not shown). Also, very high signal-to-noise ratios in the 2D HA(CACO)N spectra are required in order to obtain a sufficiently low error in the intensity ratio of the spectra with and without  $^2H^N$  decoupling. Therefore, at present it is not yet possible to apply the methodology described in this manuscript in a routine manner to a wide range of proteins. It is primarily restricted to proteins with favorable NMR characteristics, such as ubiquitin and other low molecular weight proteins. Measurement of QCC values is not restricted to amides involved in weak “structural” hydrogen bonds and is, for example, also applicable to the study of strongly hydrogen bonded N–H groups in the active sites of enzymes. The much larger variation in QCC values expected for such cases alleviates the requirement for very high signal-to-noise ratios and may make this approach applicable to a variety of systems of practical interest.

## EXPERIMENTAL

All NMR experiments were performed on a sample of uniformly  $^{13}C/^{15}N$ -labeled human ubiquitin (VLI Research, Southeastern, PA). Dry powder protein, 3.5 mg, was dissolved in 220  $\mu$ l  $D_2O$  buffered with 30 mM sodium acetate (deuterated), pH 4.7 (uncorrected meter reading), and placed in a Shigemi microcell (Shigemi Inc., Allison Park, PA). Experiments were carried out on a Bruker AMX-600 operating at a  $^1H$  resonance frequency of 600 MHz and equipped with a triple-resonance pulsed field gradient probehead. All spectra were recorded at 25°C.

The reference and attenuated spectra were collected in an interleaved manner using the pulse sequence shown in Fig. 2. Pertinent timing parameters are provided in the figure legend. The total data acquisition time per pair of spectra was 19 h. Experiments were repeated four times, several months apart, with total durations of the CPMG relaxation period of 90.9, 127.3, 145.5, and 145.5 ms, each time using  $2\xi$  durations of 9 ms. The strength of the  $^2H^N$  decoupling field was 1.7 kHz. No measurable change in  $^{15}N$   $T_2$  was detected when the decoupling field strength exceeded 800 Hz, but to ensure that the effect of imperfect  $^2H^N$  decoupling

was minimal, it was set to 1.7 kHz during the duration of the CPMG period. No improvement upon including WALTZ-16 modulation of the decoupling field was observed; in fact, at lower  $^2H^N$  decoupling power levels the introduction of WALTZ-16 modulation lowers the decoupling efficiency, presumably because the duration of a  $^2H^N$  90° pulse is comparable to the  $^{15}N$   $T_2$  and  $T_1$  values.

Both the attenuated and reference spectra were acquired as  $416^* (t_1) \times 768^* (t_2)$  data matrices (where  $n^*$  refers to  $n$  complex data points) with acquisition times of 266 ms ( $t_1$ ,  $^{15}N$ ) and 80 ms ( $t_2$ ,  $^1H^\alpha$ ). Prior to Fourier transformation, the data were apodized in both dimensions with a squared sine-bell function shifted by 72°, and then zero-filled to 2048\* along  $t_1$  and 4096\* along  $t_2$  to yield digital resolutions of 0.8 and 2.3 Hz, respectively. Data were processed using the program nmrPipe (36) and peak positions were determined interactively using the program PIPP (37).

Calculations of the evolution of  $^{15}N$ – $\{^2H\}$  coherence and relaxation during the CPMG pulse train were carried out with the program package Mathematica (Wolfram Inc., Champaign, IL).

## ACKNOWLEDGMENTS

We thank Frank Delaglio and Dan Garrett for developing the software used to process and analyze the NMR data, Stephan Grzesiek, Nico Tjandra, John Marquardt, Jin-Shan Hu, Marcel Ottiger, John Kuszewski, Marius Clore, Dennis Torchia, Angela Gronenborn, Attila Szabo, Fred Dyda, Robert Tycko, and David Davies for stimulating discussions, and Rolf Tschudin for technical assistance. This work was supported by the AIDS Targeted Anti-Viral Program of the Office of the Director of the National Institutes of Health. A.C.L. is supported by American Cancer Society Postdoctoral Fellowship PF-4030.

## REFERENCES

1. G. A. Jeffrey and W. Saenger, “Hydrogen Bonding in Biological Structures,” Springer-Verlag, New York (1991).
2. A. Fersht, “Enzyme Structure and Mechanism,” second ed., W. H. Freeman, New York, 1985.
3. A. Hvidt and S. O. Nielsen, *Adv. Prot. Chem.* **21**, 287 (1966).
4. G. Wagner, *Q. Rev. Biophys.* **16**, 1 (1983).
5. S. W. Englander and N. R. Kallenbach, *Q. Rev. Biophys.* **16**, 521 (1984).
6. J. B. Udgaonkar and R. L. Baldwin, *Proc. Natl. Acad. Sci. USA* **87**, 8197 (1990).
7. G. Wagner, A. Pardi, and K. Wüthrich, *J. Am. Chem. Soc.* **105**, 5948 (1983).
8. N. Tjandra and A. Bax, *J. Am. Chem. Soc.* in press.
9. K. Ōsapay and D. A. Case, *J. Am. Chem. Soc.* **113**, 9436 (1991).
10. E. A. C. Lucken, “Nuclear Quadrupole Coupling Constants,” Academic Press, New York (1969).
11. M. Rinné and J. Depireux, “Advances in Nuclear Quadrupole Resonance” (J. A. S. Smith, Ed., Vol. 1, Heyden, New York (1974).
12. G. Soda and T. Chiba, *J. Chem. Phys.* **50**, 439 (1969).
13. M. J. Hunt and A. L. Mackay, *J. Magn. Reson.* **22**, 295 (1976).

14. M. G. Usha, W. L. Peticolas, and R. J. Wittebort, *Biochemistry* **30**, 3955 (1991).
15. R. Gerald II, T. Bernhard, U. Haeberlen, J. Rendell, and S. Opella, *J. Am. Chem. Soc.* **115**, 777 (1993).
16. C. A. Michal, J. C. Wehman, and L. W. Jelinski, *J. Magn. Reson. B* **111**, 31 (1996).
17. J. Boyd, T. K. Mal, N. Soffe, and I. D. Campbell, *J. Magn. Reson.* **124**, 61 (1997).
18. D. R. Muhandiram, T. Yamazaki, B. D. Sykes, and L. E. Kay, *J. Am. Chem. Soc.* **117**, 11,536 (1995).
19. S. Vijay-Kumar, C. E. Bugg, and W. J. Cook, *J. Mol. Biol.* **194**, 531 (1987).
20. N. Tjandra, S. E. Feller, R. W. Pastor, and A. Bax, *J. Am. Chem. Soc.* **117**, 12,562 (1995).
21. S. Grzesiek and A. Bax, *J. Am. Chem. Soc.* **116**, 10,196 (1994).
22. R. E. London, D. M. LeMaster, and L. G. Werbelow, *J. Am. Chem. Soc.* **116**, 8400 (1994).
23. M. Ikura, L. E. Kay, and A. Bax, *Biochemistry* **29**, 4659 (1990).
24. A. C. Wang, S. Grzesiek, R. Tschudin, P. J. Lodi, and A. Bax, *J. Biomol. NMR* **5**, 376 (1995).
25. S. Meiboom and D. Gill, *Rev. Sci. Instrum.* **29**, 688 (1958).
26. I. Solomon, *Phys. Rev.* **99**, 559 (1955).
27. A. Abragam, "The Principles of Nuclear Magnetism," p. 314, Oxford Univ. Press, London (1961).
28. A. Abragam, "The Principles of Nuclear Magnetism," p. 309, Oxford Univ. Press, London (1961).
29. A. G. Redfield, *Adv. Magn. Reson.* **1**, 1 (1965).
30. G. Lipari and A. Szabo, *J. Am. Chem. Soc.* **104**, 4546 (1982).
31. M. Windholz (Ed.), "The Merck Index Ninth Edition," p. 385, Merck, Rahway, NJ (1976).
32. N. Tjandra, S. Grzesiek, and A. Bax, *J. Am. Chem. Soc.* **118**, 6264 (1996).
33. A. Brünger, "X-PLOR Version 3.1: A System for X-ray Crystallography and NMR," Yale Univ. Press, New Haven (1992).
34. E. R. Henry and A. Szabo, *J. Chem. Phys.* **82**, 4753 (1985).
35. A. C. LiWang and A. Bax, *J. Am. Chem. Soc.* **118**, 12,864 (1996).
36. F. Delaglio, S. Grzesiek, G. W. Vuister, G. Zhu, J. Pfeifer, and A. Bax, *J. Biomol. NMR* **6**, 277 (1995).
37. D. S. Garrett, R. Powers, A. M. Gronenborn, and G. M. Clore, *J. Biomol. NMR* **4**, 376 (1995).